

High-throughput single-vesicle imaging platform for direct extracellular vesicle profiling of human plasma

Received: 9 August 2025

Accepted: 9 April 2026

Cite this article as: Han, C., Melkonian, A.V., Rolando, J.C. *et al.* High-throughput single-vesicle imaging platform for direct extracellular vesicle profiling of human plasma. *Nat Commun* (2026). <https://doi.org/10.1038/s41467-026-72179-0>

Chungmin Han, Arek V. Melkonian, Justin C. Rolando, Sara Whiteman & David R. Walt

We are providing an unedited version of this manuscript to give early access to its findings. Before final publication, the manuscript will undergo further editing. Please note there may be errors present which affect the content, and all legal disclaimers apply.

If this paper is publishing under a Transparent Peer Review model then Peer Review reports will publish with the final article.

High-throughput single-vesicle imaging platform for direct extracellular vesicle profiling of human plasma

Chungmin Han (1,2,3), Arek V. Melkonian (1,2,3), Justin C. Rolando (1,2,3), Sara Whiteman (1), and David R. Walt (1,2,3)#

(1) Wyss Institute for Biologically Inspired Engineering, Boston, MA, USA

(2) Department of Pathology, Brigham and Women's Hospital, Boston, MA, USA

(3) Harvard Medical School, Boston, MA, USA

#corresponding authors: dwalt@bwh.harvard.edu

Abstract

Extracellular vesicles (EVs) are nanoscale particles secreted by cells that carry diverse biomolecules reflecting their cell of origin. Single-EV imaging approaches have enabled precise characterization of heterogeneous EV populations; however, their broader application is limited by low-throughput workflows and cumbersome EV isolation procedures. Here, we introduce a streamlined, high-throughput imaging platform capable of analyzing protein expression of individual intact EVs directly from unprocessed biological samples at the single-vesicle level. Our approach employs a functionalized glass surface optimized for high-throughput single-EV imaging, facilitating specific capture of EVs and enabling integration with existing automation technologies. We evaluate the platform's analytical capabilities by characterizing various recombinant EV samples and demonstrate their clinical utility by analyzing EVs in a total of 191 human plasma samples with high-throughput efficiency. This technology will offer a pathway for high-precision and large-scale characterization of EVs in clinical samples.

Introduction

Extracellular vesicles (EVs) are nano-sized, lipid-enclosed sacs released by almost all cell types, which likely have critical roles in intercellular communication by transporting diverse biomolecules from their cells of origin^{1,2}. Owing to their unique characteristics, EVs have received significant attention for their potential roles in mediating biological activities such as immune regulation, as well as for their potential clinical applications in diagnostics and as delivery vehicles for therapeutics³⁻⁵. However, accurate characterization of EVs remains challenging due to their small size and intrinsic heterogeneity; even EVs secreted by a single cell line consist of multiple subpopulations with distinct molecular and biophysical features⁶⁻⁸. Most conventional EV analyses rely on bulk measurement techniques that require lysis of heterogeneous EVs, thereby destroying vesicular structure and obscuring individual features by averaging information across different EV subpopulations⁹.

A variety of single-EV imaging approaches have been developed to address the limitations of conventional bulk approaches^{10,11}. Diffraction-limited fluorescence microscopies, such as

confocal and total-internal reflection microscopies, have emerged as the most widely utilized platforms for analyzing individual EVs^{12,13}. More advanced platforms incorporate super-resolution microscopies, microfabricated substrates, plasmonic enhancement strategies, or clickable fluorescence probes to improve resolution, sensitivity, and multiplexing capability^{14–16}. These technologies have provided valuable insights into single-EV protein expression and phenotypic diversity at the single-EV level, significantly improving our understanding of EV heterogeneity and demonstrating the value of single-EV analysis.

Despite these advances, several practical challenges limit the broader application of current single-EV technologies^{17,18}. Super-resolution and other advanced imaging modalities often require long acquisition times and extensive image processing, restricting the number of EVs or samples that can be analyzed¹⁹. Commercial platforms, such as nanoflow cytometry and ExoView, enable efficient single-EV analysis without requiring specialized expertise; however, these approaches rely on dedicated instrumentation or proprietary microfabricated substrates, which may limit accessibility, flexibility, or scalability depending on the application. In addition, some single-EV workflows rely on pre-isolated EVs, typically prepared using ultracentrifugation or size-exclusion chromatography (SEC), which may reduce throughput, introduce variability, and complicate large-scale studies^{20,21}. Consequently, many single-EV methods are used primarily for qualitative or small-scale analyses, and their throughput can be limiting for analytical or translational applications that require the measurement of large sample cohorts (e.g., on the order of 100 samples)²².

In this study, we introduce a streamlined, high-throughput (HT) single-EV imaging platform developed to address throughput limitations and provide a tool for quantitative analysis of large sample sets. The platform integrates an optimized, highly reproducible PEG-based surface functionalization strategy compatible with standard commercial HT formats, avoiding harsh chemical conditions while maintaining stable and robust EV capture and imaging^{23,24}. EVs from unprocessed biological samples are directly captured and labeled on the surface through a workflow similar to a single-molecule pull-down assay and imaged using a conventional fluorescence microscope (**Figure 1**)²⁵. This eliminates the need for sample pre-processing, thereby reducing the variability associated with EV isolation and improving throughput. Using recombinant EVs and human plasma samples, we demonstrated that the workflow provides reproducible and linear detection of single-EV signals across a broad dynamic range. Integration with existing HT automation technologies enabled consistent analysis across 100 human plasma samples. These capabilities position the platform as a practical and scalable tool for single-EV characterization with potential for future clinical applicability.

Results

Optimization of surface functionalization for high-throughput glass-bottom formats

Ultrasensitive fluorescence imaging of individual nanoscale targets, such as single proteins or EVs, requires high-quality functionalized surfaces that enable specific target capture while minimizing NSB. For quantitative and HT analysis, the surface must also exhibit uniform performance and compatibility with existing HT platforms. To this end, we selected glass-bottom 96-well plates and 18-chambered microscope slides as our imaging substrates and developed an

optimized surface functionalization method tailored for their use (**Figure 1**). We adapted a one-step PEGylation method using PEG-silane to reduce batch-to-batch variability commonly associated with conventional multi-step conjugation protocols (see **Methods**). The harsh cleaning and surface activation methods involving organic solvents or strong acids were replaced with oxygen plasma treatment to preserve the integrity of polystyrene structures in the commercial formats. To evaluate the surface passivation performance, we tested various PEG-silane conjugation conditions and assessed NSB using fluorescent EVs, antibodies (Abs), and oligo-DNAs (**Supplementary Figure 1a**).

Fluorescent EVs were produced by transiently transfecting Expi293F cells with plasmids encoding either mEmerald-tagged CD9 (mEm-CD9) or mCherry inserted into the small extracellular loop of CD9 (CD9-SEL-mCh) (**Figure 2a**). EVs in the Expi293F conditioned media were characterized according to the MISEV 2023 guideline (**Supplementary Figure 2**). Surfaces prepared with >4% (w/v) PEG-silane, followed by 1% Tween-20 and 1% BSA blocking, effectively minimized NSB of mEm-CD9-EVs ($\sim 10^{10}$ EVs/mL), as well as NSB of mAbs and oligo-DNAs at ~ 60 nM (**Supplementary Figure 1a-d**). Based on these results, we selected 4% PEG-silane as the optimal passivation condition for downstream optimization. We next optimized the biotin-PEG-silane fractions, NeutrAvidin (NA), and capture-mAb (anti-CD9 mAb) concentrations for EV capture efficiency. A biotin-PEG fraction of >1% of total PEG (e.g., 3.96% w/v mPEG-silane + 0.04% w/v biotin-PEG-silane) yielded maximal EV capture when combined with 0.2 mg/mL of NA and 2 μ g/mL of capture-mAb (**Supplementary Figure 3a-e**). Increasing NA or antibody concentrations beyond these values did not improve capture efficiency (**Supplementary Figure 3d-e**). Across all conditions, low standard deviations from nine different fields of view (FOVs) indicated consistent and homogeneous surface functionalization. Based on these findings, we established a standardized surface functionalization and EV capture protocol using 4% PEG-silane with 1% biotin-PEG fraction, 0.2 mg/mL NA, and 2 μ g/mL capture antibody as the optimal condition for HT single-EV imaging.

Implementation of a single monoclonal antibody strategy for EV-specific detection

A conventional sandwich immunoassay uses a pair of antibodies that bind distinct epitope sites of a single target molecule. However, unlike a single molecule, a single EV is a complex of biomolecules expressing multiple copies of surface EV markers (e.g., CD9), allowing for an alternative detection strategy²⁶. By exploiting the multiple copies, we implemented a single-mAb approach in which the same mAb against CD9 is used for both capture and detection. This approach selectively detects EVs bearing two or more copies of CD9 while excluding soluble, non-EV-bound forms of CD9 that cannot simultaneously bind to the two same anti-CD9 mAb (**Figure 2b**). To validate this EV-specific detection strategy, we prepared a mixture of recombinant soluble CD9 (CD9-His) and mEm-CD9-EVs. The anti-CD9 mAb was conjugated to CF647 for detection, and the anti-His detector-mAb was conjugated to CF568 to simultaneously visualize the soluble CD9-His. We successfully demonstrated that $\sim 99\%$ of mEm-CD9-EVs (blue) captured by a CD9-capture surface were detected with the CF647-labeled anti-CD9 mAb (green) based on the mEmerald and anti-CD9 detector (green) signal colocalization (**Figure 2c, d**). In contrast, soluble CD9-His capture by the CD9-capture surface was not detected by the same anti-CD9 detector mAb (<0.2% colocalization between CF567 anti-His mAb and CF647 anti-CD9 mAb), confirming the

specificity of the single anti-CD9 mAb approach for a specific EV capture and detection (**Figure 2c, d**). Additionally, the detection of single CD9-His molecules by the anti-His mAb signal (red) confirms that the optimized surface and current imaging setup are sensitive enough to detect single protein molecules captured on the surface.

Evaluation of surface marker-specific capture of EVs in unprocessed plasma

We next evaluated whether our single-EV imaging analysis could directly analyze a specific EV population from unprocessed biological samples. To simulate this, we spiked varying amounts of CD9-SEL-mCh-EVs into a 10-fold diluted human plasma sample. The spiked-in samples were analyzed using surfaces with either anti-mCherry capture-mAbs or anti-CD9 capture-mAbs, in combination with anti-CD9-CF647 detector-mAbs (**Figure 2e**). In this configuration, the spiked-in CD9-SEL-mCh-EVs will be detected as colocalized mCherry (red) and anti-CD9 detector-mAb (green) signals, while endogenous plasma-derived CD9⁺ EVs will only show the anti-CD9 detector-mAb (green) signals (**Figure 2e**). The anti-mCherry capture surface demonstrated specific capture of the CD9-SEL-mCh-EVs even in the presence of abundant plasma-derived CD9⁺ EVs in the sample, whereas the anti-CD9 capture surface captured both spiked-in and plasma-derived EVs (**Figure 2f-h**). NSB of plasma-derived EVs on the anti-mCherry capture surface was low (<5% of total detected EVs) across all conditions, confirming the specificity of the targeted capture (**Figure 2g**). Notably, the number of detected CD9-SEL-mCh-EVs was lower on the anti-CD9 capture surface than on the anti-mCherry capture surface (e.g., 525 vs. 1,353 counts per field for the 1% mCh-EV spike-in sample), suggesting a competition between spiked-in EVs and endogenous plasma EVs for binding to the anti-CD9 capture antibody (**Figure 2g, h**). Nevertheless, the relative ratio between detected CD9-SEL-mCh-EVs and plasma-derived EVs closely mirrored the actual spike-in proportions, indicating that the assay accurately captured the composition of mixed EV populations. For example, the detected CD9-SEL-mCh-EV to plasma-derived EV ratio was 56% for the 10% plasma + 1% mCh-EV, 5.2% for 0.1% mCh-EV, and 0.6% for 0.01% mCh-EV spike-in conditions (**Figure 2h**). Furthermore, we confirmed that the performance of the target-specific detection was unaffected by plasma content up to 10% (v/v), again indicating a robust passivation performance in complex biological matrices (**Supplementary Figure 4**).

Optimization and characterization of EV capture efficiency

Detection sensitivity is another important feature for single-EV analysis. Based on our optimized surface conditions, we further enhanced the EV capture by introducing shaking during the EV incubation step. Considering the relatively slow diffusion of large EV particles compared to small soluble molecule targets, we hypothesized that active mixing would improve the EV capture efficiency (**Supplementary Figure 5a**). Shaking the chambers at 700 RPM during the 10 min EV incubation increased the number of detected EVs by ~3-fold (**Supplementary Figure 5b, c**). Extending the shaking duration to 60 min further improved capture efficiency, resulting in a ~2-fold increase relative to the 10 min shaking condition and an overall ~6-fold increase compared to the static 10 min incubation (**Supplementary Figure 5c**).

To quantitatively assess the capture efficiency of EVs, we measured CD9 concentration before and after the EV capture using an orthogonal, ultrasensitive single-molecule array (Simoa) assay (**Figure 3a**). We evaluated the EV capture efficiency of the anti-CD9 surface and control surface with no capture-mAb to characterize both specific capture and non-specific loss of EVs by adsorption to plastic surfaces or during liquid handling. Under the optimized conditions, ~60 to 80% of the input mEm-CD9-EVs were captured after accounting for non-specific losses, across an input EV range of 10^8 to 10^{10} particles/mL (**Figure 3b**). At lower input EV concentrations ($<10^6$ particles/mL), the CD9 concentration of unbound EVs in the supernatant was below the detection limit of the Simoa assay. Capture efficiency was also determined by comparing the number of EVs detected on the surface with the total number of EVs added. The analysis suggested that the anti-CD9 surface captured ~6% of 2.25×10^7 mEm-CD9-EVs, estimated based on the particle counts measured by nanoparticle tracking analysis (NTA) (**Supplementary Table 1**). However, these values should be interpreted as approximate and sample-dependent, as the total number of EVs added cannot be precisely defined and may vary substantially depending on sample source, processing conditions, and the measurement modality used to estimate EV concentration²⁷.

Characterization of the analytical sensitivity of the single-EV imaging analysis

We next evaluated the analytical sensitivity of the single-EV imaging analysis. To determine the detection limit and the dynamic range, a mEm-CD9-EV sample with a predetermined concentration (2.3×10^{11} EVs/mL by NTA) was serially diluted over a wide range of concentrations and analyzed (**Figure 3c**). We observed a wide dynamic range of mEm-CD9-EV detection spanning ~4 orders of magnitude, from 2.2×10^5 to 3.6×10^9 particles/mL, with a lower limit of detection (LOD) of 2.8×10^4 particles/mL (**Figure 3d, e** red line). In comparison, a bulk intensity-based measurement of the same samples showed a much narrower dynamic range of < 2 orders of magnitude, from 9.0×10^8 - 5.8×10^{10} particles/mL, with a significantly higher LOD of 6.5×10^8 particles/mL (**Figure 3d, e** blue line). Although the bulk analysis covered a higher concentration range, the single-EV detection demonstrated approximately a 10,000-fold lower LOD and a notably broader dynamic range²⁸.

Automation of single-EV imaging analysis and evaluation of reproducibility

To enhance throughput and reproducibility of the analysis, we automated the single-EV imaging workflow by integrating it with a liquid handling robot and a motorized microscope (**Figure 4a**). The entire workflow, including reagent loading, incubation, and washing, was automated using the Tecan Fluent 780 liquid handling system equipped with a HydroSpeed plate washer and BioShake plate shakers²⁹. The system can process 96 samples in a 96-well plate in ~2 hours without requiring any human intervention during operation. Following the automated assay preparation, the prepared plate can be automatically imaged using a Nikon Ti2E microscope equipped with a motorized stage and a Perfect Focus System (PFS). Image acquisition was fully automated via a Python-based script using the Pycro-Manager package, which can acquire 49 FOV of single-EV images per well (a total of 4,704 single-channel images per plate) in less than 1 hour³⁰. The acquired single-EV images were processed using a combination of ImageJ and Python scripts, employing the ThunderSTORM ImageJ plugin for single-EV spot detection and the quantitative

analysis of single-EV fluorescence signals³¹. Processing 4,704 images to extract average EV counts per field required less than 1 hour on a standard computer.

To assess the reproducibility of the automated workflow, we analyzed a mEm-CD9 EV sample across all 96 wells of a plate. Intra-well variability was first evaluated by acquiring 169 images across a single well from the center of the well (**Supplementary Figure 6a**). The results showed a concentration gradient within the well due to the surface tension and meniscus effect, with lower EV counts in the center and higher counts near the edges. Based on this observation, we determined that acquiring 25 to 81 FOV from the center of a well provides a representative estimate of average EV counts per well (**Supplementary Figure 6b**). Thus, all subsequent analyses using the automated single-EV analysis platform acquired 25 or 49 FOV per well. The analysis showed excellent intra-plate reproducibility across the entire 96-well plate with a coefficient of variation (CV) of ~3.89%: heatmap visualization did not show any biases across the plate, including the edges (**Figure 4b, c**; Plate 1). Repeating the experiment on a second plate yielded nearly identical results, with almost identical mean EV counts (240.5 vs. 243.0) and CVs (3.89% vs. 4.87%) with no statistically significant difference between the plates (two-sided t-test, $p = 0.1353$), indicating excellent inter-plate reproducibility (**Figure 4c**).

Baseline EV counts in normal human plasma samples

We then characterized CD9⁺ EV and CD81⁺ EV counts in plasma samples from 96 normal individuals to verify baseline CD9⁺ EV and CD81⁺ EV counts in normal human plasma. Before analyzing the full cohort, we first analyzed three pooled normal human plasma samples under various control conditions to confirm that plasma EVs could be reliably detected without significant background interference. Control surfaces without capture-mAbs or with isotype control mAbs effectively suppressed NSB of both EVs and detector-mAbs when tenfold-diluted plasma samples were used (**Figure 4d, e**). In contrast, the surface coated with anti-CD9 capture and detector-mAbs yielded distinct CD9⁺ EV signals from all three pooled plasma samples (**Figure 4d, e**). Together with the previous spike-in experiments, these results demonstrate that the single-EV analysis can be directly performed using unprocessed or minimally processed plasma samples without the need for prior EV isolation or enrichment (**Figure 2e-h, 4d, e**).

To further assess the nature of the detected signals, detergent treatment experiments were performed. Treatment of the surface-captured human plasma-derived EVs with 0.05% Triton X-100 substantially reduced the number of CD9⁺ signals by ~75% compared to the untreated or Tween-20 (0.05%) treated samples (**Supplementary Figure 7**). In addition, the remaining ~25% of detected signals after the Triton X-100 treatment exhibited significantly reduced fluorescence intensity, with CD9 intensity decreased to ~10% of those measured in the untreated or Tween-20 conditions (**Supplementary Figure 7**). This observation suggests that the majority of CD9 signals detected from the human plasma analysis originate from EV-associated structures whose membrane structure can be disrupted by the Triton X-100 treatment. Although treatment with 0.05% Tween-20 did not produce significant changes in CD9⁺ EV detection in our analysis, prior studies have raised concerns regarding the potential effect of Tween-20 on EV membrane integrity³²[NO_PRINTED_FORM]. Therefore, the use of Tween-20 in buffers should be avoided in applications where the membrane integrity of EVs is critical, such as luminal cargo analysis.

The 96 normal human plasma samples represented a diverse population with nearly equal numbers of females and males, ages ranging from 18 to 61 years, and body mass indices (BMIs) ranging from 18 to 59 (**Supplementary Table 2**). For analysis, 10 μL of thawed plasma was directly transferred to anti-CD9 or anti-CD81 capture plates containing 90 μL of PBS, resulting in a final tenfold dilution of the samples without any prior centrifugation or filtration. All samples were co-analyzed with an isotype detector-mAb as an internal control. The analysis successfully detected CD9⁺ EVs and CD81⁺ EVs from all plasma samples. The average EV counts from tenfold-diluted plasma were $\sim 1,070$ counts per field for CD9⁺ EVs and $\sim 1,011$ counts per field for CD81⁺ EVs (**Figure 4f**). The difference between CD9⁺ and CD81⁺ EV counts was not statistically significant (Mann-Whitney U test: $U = 2847$, $p = 0.3092$), and biological variations between the samples were relatively high (CV=34.5% for CD9⁺ EVs and CV=49.3% for CD81⁺ EVs) (**Figure 4f**).

To assess whether clinical covariates affected the baseline CD9⁺ and CD81⁺ EV counts, we performed Spearman correlation and multiple linear regression (MLR) analyses using age, sex, and BMI as predictors (**Figure 4g, Supplementary Tables 3**). Neither CD9⁺ nor CD81⁺ EV counts were significantly associated with these variables. Although CD81⁺ EVs showed a statistically significant correlation with sex in both analyses, the correlation coefficient (ρ) and the MLR effect size were small (**Figure 4g, Supplementary Table 3**). In contrast, a moderate and statistically significant positive correlation was observed between CD9⁺ and CD81⁺ EV counts (Spearman $\rho = 0.56$, $p < 0.001$) (**Figure 4g**).

Approximately 20% of the samples (18 of 96) showed elevated background from the isotype control mAb (> 200 counts per field) (**Supplementary Figure 8a, b**). However, CD9⁺ and CD81⁺ EV counts were not significantly affected and showed no difference between the low- and high-background groups (**Supplementary Figure 8c**). All plasma samples were further analyzed for common plasma confounding factors such as hemolysis (A410), lipemia (A700), icterus (A450), and total protein concentration (A280) to identify potential causes of high background. None of these parameters showed statistically significant correlations with background levels (**Supplementary Table 2, Supplementary Figure 8d**). These results confirmed that high background did not biologically or statistically confound the analyses; therefore, we included all the samples for subsequent analyses.

Elevation of CD9⁺ and CD81⁺ EV levels in breast cancer patient plasma samples

Next, we evaluated how breast cancer influences plasma levels of CD9⁺ and CD81⁺ EVs. Normal and breast cancer plasma samples were collected from two different sites and combined with normal female plasma samples from the previous normal plasma sample analysis (**Figure 5a**). All samples were from female donors; different disease stage samples were not matched for age or BMI because our normal plasma sample analysis showed no significant correlation between CD9⁺ or CD81⁺ EV counts and age or BMI (**Figure 4g, Supplementary Table 3**). To evaluate whether the differences in plasma collection and processing procedures across cohorts introduced biases in analysis, we first compared the CD9⁺ EV counts between 50 normal plasma samples from BioIVT and 18 normal plasma samples from the MGB biobank. No statistically significant difference in CD9⁺ EV detection was observed between the groups, indicating that the influence of different plasma handling processes in our cohort is minimal (**Supplementary Figure 9**). The

final sample cohort included 68 normal, 27 early-stage breast cancer (stage I/II), and 46 late-stage breast cancer (stage III/IV) plasma samples (**Figure 5a**).

The samples were analyzed for CD9⁺ and CD81⁺ EV counts using the automated HT single-EV analysis platform. The resulting EV counts were plotted in descending order as color-coded bar graphs, with normal, early-stage, and late-stage samples represented in blue, orange, and brown, respectively (**Figure 5b, c**). While plasma CD9⁺ EV counts showed a wider variation (896-7,270 counts per field) with a clear separation between the normal and late-stage groups, the plasma CD81⁺ EV counts did not show such elevation in EV counts or separation across disease stage. A Kruskal-Wallis test showed a statistically significant difference in CD9⁺ EV counts across the three groups ($p < 0.001$), and Dunn's post-hoc test showed that the CD9⁺ EV counts were significantly elevated in late-stage breast cancer compared to early-stage breast cancer (adjusted $p < 0.001$) and normal controls (adjusted $p = 0.002$) (**Figure 5d**). Receiver operating characteristic (ROC) analysis was performed to evaluate the diagnostic performance of plasma CD9⁺ EV counts (**Figure 5e**). The area under the curve (AUC) value between the normal and late-stage groups was ~ 0.86 , indicating robust differentiating power, whereas the AUC values between the early- and late-stage groups (~ 0.74) and the normal and early-stage groups (~ 0.65) indicated less effective performance. Confusion matrix analyses of plasma CD9⁺ EV counts between the disease stages also agreed with the ROC AUC analysis (**Supplementary Figure 10a-c**). In contrast, although the statistical analysis of plasma CD81⁺ EV counts also showed a statistically significant difference between normal and late-stage groups (adjusted $p < 0.001$), ROC analysis of plasma CD81⁺ EV counts showed substantially lower discriminative performance compared to plasma CD9⁺ EV counts (**Figure 5f, g**). Confusion matrix analyses of CD81⁺ EV counts again reflected overall lower performance (**Supplementary Figure 10d-f**).

Identification of potential origin of elevated CD9⁺ EVs in breast cancer plasma

To further investigate whether the elevated CD9⁺ EV counts observed in late-stage breast cancer plasma originated from tumor-derived EVs, we performed multiplexed single-EV colocalization analyses for CD9 with breast cancer-associated surface markers. First, EVs derived from the HER2-positive breast cancer cell line SK-BR-3 and from noncancerous Expi293F cells were analyzed for HER2, HER4, TROP2, or PD-L1 expression on anti-CD9 capture surface. HER2⁺ and TROP-2⁺ EVs were clearly detected in SK-BR-3 EVs, whereas HER4⁺ and PD-L1⁺ EVs were almost not detected in either EV sample (**Supplementary Figure 11a-c**). Importantly, the association of HER2 and TROP-2 with CD9⁺ EVs showed a higher statistical significance when analyzed by colocalization analysis than by single-marker quantification (adjusted $p = 0.227$ for HER2 single-marker and adjusted $p = 0.006$ for HER2 colocalization using SK-BR-3 EVs, Kruskal-Wallis test with Dunn's post hoc) (**Supplementary Figure 11b, d**).

Based on these observations from cell-derived EV, we next analyzed plasma samples from breast cancer patients (Cohorts 2 and 3) to determine whether tumor-associated HER2⁺ or TROP-2⁺ EVs contributed to the elevated CD9⁺ EV levels observed in late-stage disease. In single-marker analyses, a subset of late-stage samples showed elevated HER2⁺ (9 of 46 samples) and TROP-2⁺ (14 of 46 samples) EV counts above the LOD (**Supplementary Figure 11f, g**). TROP-2⁺ EVs were significantly elevated in late-stage breast cancer compared with the normal samples (adjusted $p = 0.003$, Kruskal-Wallis with Dunn's post hoc), whereas HER2⁺ EVs did not show significant

differences between groups (**Supplementary Figure 11f, g**). Following colocalization analyses with CD9 showed neither CD9-HER2 nor CD9-TROP-2 double-positive EV populations were significantly elevated in late-stage disease (adjusted $p > 0.9$ for all comparisons) (**Supplementary Figure 11h, i**). Together, these results suggest that while the number of CD9-HER or CD9-TROP-2 double-positive EVs may increase in late-stage disease because of the overall rise in CD9⁺ EVs, their relative proportion within the total CD9⁺ EV population remains unchanged.

Discussion

Single-EV imaging technologies such as the single-particle interferometric reflectance imaging sensor (SP-IRIS/ExoView), diffraction-limited microscopy, and super-resolution microscopy have substantially transformed EV characterization by visualizing molecular features of EVs at the individual particle level. However, the broader application of these platforms, particularly for large-scale or clinical applications, has been restricted by their limitations in throughput and accessibility. Many commercial platforms rely on proprietary chips or dedicated instrumentation, which restricts flexibility in assay development and the number of samples analyzed. Super-resolution approaches, including single-molecule localization microscopy, demonstrated true nanoscale resolution for single-EV detection but require long acquisition times and extensive image processing, making them inherently low throughput and unsuitable for quantitative analysis across large sample sets.

To address these limitations, we developed an HT single-EV imaging platform for a reliable and quantitative EV detection across large sample sets. As part of creating this platform, we first optimized a one-step PEGylation method adapted from the gold-standard single-molecule fluorescence microscopy surface to be compatible with HT glass-bottom plastic formats. We confirmed that the strategy provides consistent and reliable background suppression and EV capture across the surfaces within and between batches. We then applied the method to an HT 96-well plate format, enabling the analysis of thousands to hundreds of thousands of individual EVs per sample across hundreds of samples under consistent surface conditions. Leveraging these improvements, we rigorously characterized the analytical performance of the platform. The platform achieved high detection sensitivity and a broad dynamic range through single-EV detection, rather than bulk-averaged measurements, consistent with our previous work using a digital single-molecule assay²⁸.

Furthermore, the single mAb capture and detection workflow enables direct analysis of EVs in unprocessed plasma samples with high specificity and minimal background interference, minimizing the need for prior EV isolation. Although this approach may still risk misidentifying lipid fragments or protein aggregates carrying multiple copies of target antigens as EV signals, our plasma spike-in and crude plasma sample analyses indicate that such non-vesicular interference is minimal under typical assay conditions. We also demonstrated multiplexed detection that enables colocalization analysis. By incorporating secondary markers, such as mCherry or TROP-2, and analyzing their colocalization with canonical EV markers, such as CD9, we were able to successfully distinguish spiked-in mCherry⁺ EVs from plasma-derived EVs and EV-associated TROP-2 signals from non-EV-associated signals. This multi-marker colocalization approach could substantially improve both accuracy and interpretability without requiring additional purification. Nevertheless, for applications that prioritize high specificity over throughput, additional isolation

steps such as SEC or filtration may still be required.

The major strength of the platform is its compatibility with standard laboratory automation technologies. Integration with liquid-handling robotics and a motorized fluorescence microscope enabled analysis of hundreds of samples per day, representing an unprecedented throughput for single-EV analysis. Automation not only improves throughput but also enhances reproducibility by minimizing human variability. The precision obtained using 96 technical replicates demonstrated a CV below 4%, which is ideal for detecting subtle biological differences. Notably, the workflow can still be performed reliably even without automation, using multi-channel pipettes and plate washers, within a similar time frame as a standard ELISA.

To further demonstrate our platform's utility, we profiled CD9⁺ and CD81⁺ EV levels in plasma samples from 96 normal individuals. No significant associations were observed between baseline CD9⁺ and CD81⁺ EV levels and common demographic factors such as age, sex, and BMI, and only a moderate positive correlation was observed between CD9⁺ and CD81⁺ EV counts ($\rho = 0.56$, $p < 0.001$). However, previous studies using NTA and various EV isolation techniques have reported inconsistent observations regarding the influence of demographic factors on baseline EV levels^{33,34}. For example, an NTA-based study utilizing density gradient ultracentrifugation and SEC reported no correlation between EV levels and demographic factors in 35 healthy individuals³⁵. Conversely, another study using NTA with polymer precipitation and ultracentrifugation in 74 individuals found negative correlations with age and positive correlations with BMI³⁶. These discrepancies likely reflect methodological differences, particularly because NTA measures all nanoparticles nonspecifically, including lipoproteins. Advanced single-EV analyses that can characterize defined EV populations may help address this challenge. Although we did not fully resolve these discrepancies in this study, we expect our HT single-EV analysis platform to enable reproducible and large-scale characterization of EVs in clinical samples in the future.

Changes in circulating EV levels associated with disease have been reported in the literature, with cancer being the most extensively investigated due to tumor cells typically secreting significantly more EVs compared to healthy cells³⁷⁻³⁹. However, reports on elevated circulating EV levels in cancer patients remain inconsistent. For example, some NTA-based studies reported increased circulating EV levels in patients with glioblastoma and pancreatic cancer, whereas others found no significant elevation in melanoma, breast cancer, or other solid tumors⁴⁰⁻⁴⁴. Although certain reports suggested that specific EV subpopulations expressing tumor biomarkers were elevated in blood, these findings were not consistently reported⁴⁵. In contrast, animal studies consistently demonstrated positive correlations between circulating EV levels and tumor growth^{41,42,46}. Additionally, a mathematical modeling study using animal data suggested a direct correlation between tumor burden and circulating EV levels⁴⁷. Therefore, again, the discrepancies in human studies likely arise not only from biological variability but also from methodological limitations as discussed above.

Using our high-throughput single-EV analysis platform, we observed the elevation of CD9⁺ EVs in plasma samples from breast cancer patients, whereas CD81⁺ EV levels remained largely unchanged. Given the moderate correlation between CD9⁺ and CD81⁺ EV counts in normal individuals, this selective elevation of CD9⁺ EVs suggests enrichment of specific EV phenotypes potentially linked to tumor or tumor-associated sources. However, our colocalization analyses

revealed that the fraction of CD9-HER2 and CD9-TROP-2 double-positive EV populations remained unchanged in late-stage patients' plasma, indicating that their contribution to the elevation of plasma CD9⁺ EV in late-stage disease might be minimal. This is consistent with previous reports indicating that tetraspanins, including CD9, are widely expressed across diverse cell types and may not serve as tumor-specific markers⁴⁸. Instead, these observations suggest that the elevation of CD9⁺ EV levels in plasma may reflect broader systemic changes in EV biogenesis, release, or clearance associated with tumor progression or host immune response. While our current study does not provide definitive evidence to resolve the ongoing controversy regarding the origins of circulating EVs in cancer, the single-EV platform offers an important means to gain both mechanistic and methodological insights into this question.

It is important to note that our platform currently does not provide absolute EV concentrations (i.e., particles/mL), primarily due to the absence of EV reference materials suitable for generating calibration curves. Although recombinant mEm-CD9-EVs were valuable for proof-of-concept demonstrations, inherent differences between recombinant EVs and endogenous human plasma-derived CD9⁺ EVs prevent accurate quantification of absolute EV numbers in plasma samples. Thus, further study is needed to identify suitable reference materials for generating reliable standard curves in single-EV analyses, acknowledging that typical recombinant protein standards may also not adequately reflect the complex properties of intact EV particles.

In summary, we developed and validated an automatable HT single-EV imaging platform that provides highly consistent, sensitive, and scalable characterization of EVs directly from minimally processed plasma samples. By combining optimized PEG-based surface chemistry, compatibility with HT formats and standard laboratory automation, and comprehensive analytical validation, the platform addresses major limitations of existing single-EV technologies. Application of the platform to human plasma samples reliably identified baseline plasma CD9⁺ EV levels in normal individuals and revealed significantly elevated CD9⁺ EV levels in breast cancer patients, particularly in late-stage disease. Together, these findings demonstrate that the platform's ability to reliably analyze large sample sets makes it a powerful tool for biomarker discovery, mechanistic EV studies, and future clinical translation.

Methods

Ethics statement

We confirm that the protocols and samples used in this study comply with regulations. Protocols related to ultrasensitive detection of biomarkers for disease diagnosis were reviewed and approved by the Harvard Committee on Microbiological Safety (COMS, ID 22-051). Human plasma samples were acquired from three different sources: 100 normal human plasma samples were purchased from BioIVT, 36 normal and breast cancer patient-derived plasma samples were collected from BWH Faulkner Hospital under Partners IRB 2022P000451, and 55 breast cancer patient-derived plasma samples were acquired from the MGB BioBank under MGB IRB 2021P002215.

Affinity reagents and their conjugates

Anti-CD9 (HI9a clone, #312112 for biotinylated mAb and #312102 for purified mAb) and anti-mCherry (8C5.50 clone, #677702 for purified mAb), anti-His tag (J095G46 clone, #362611 for AF647 conjugated), and mouse IgG1 isotype control (MOPC-21 clone, #400165 for purified mAb) mAbs were purchased from Biolegends. Anti-CD81 (M38 clone, #MA562351 for biotinylated mAb and #MA5-44066 for purified mAb) mAbs were purchased for ThermoFisher. Anti-TROP2 (Sacituzumab, #HY-P99045 for purified mAb), anti-HER2 (Trastuzumab, #HY-P9907A for purified mAb), and anti-PD-L1 (Atezolizumab, #HY-P9904 for purified mAb) mAbs were purchased from MedChemExpress. Anti-HER4 (MAB1131 clone, #MAB1131 for purified mAb) was purchased from R&D Systems. The purified antibodies were biotinylated using EZ-Link™ NHS-PEG4-Biotin (A39259, ThermoFisher) for use as capture-mAbs and fluorophore-conjugated using Mix-n-Stain™ CF® Dye Antibody Labeling Kits (#92233 for CF488A, #92235 for CF568, and #92238 for CF647 conjugations, Biotium) for use as detector-mAbs according to the manufacturers' instructions.

Preparation of functionalized surface for single-EV imaging in high-throughput platforms

Commercial glass-bottom 18-chamber microscope slides (81817, ibidi) or 96-well glass-bottom microplates (P96-1.5H-N, Cellvis) were used as base platforms for surface functionalization for the single-EV imaging analysis. Treatment with oxygen plasma (50W for 2 min, Atto, Diener electronic) was utilized to activate the glass surfaces. Activated surfaces were immediately incubated with mPEG-silane and biotin-PEG-silane (MPEG-SIL-5000-5GR and BIOTIN-PEG-SIL-5000-1GR, Laysan Bio) dissolved in pH-adjusted anhydrous ethanol (pH 2.0) for at least 1 hour at room temperature (RT). The PEGylated surfaces were then washed four times with Milli-Q water and dried in a 55°C drying oven for at least 1 hour. The surfaces were vacuum sealed in food-saver bags and stored at -20°C.

Single-EV imaging assay

The overall workflow of the single-EV imaging assay is similar to a conventional sandwich-immunoassay. Both 18-chamber slide and 96-well plate formats were incubated with 100 μ L of reagents prepared in PBST-BSA (PBS pH 7.4 with 0.05% Tween-20 and 1% BSA) and washed three times with 200 μ L of wash buffer PBST (PBS pH 7.4 with 0.05% Tween-20) between the steps, unless otherwise stated. The wells with functionalized surfaces were further blocked by 1% (w/v) Tween-20 (Sigma) in PBS pH 7.4 (ThermoFisher) and then by 1% BSA (Sigma) in PBS pH 7.4, both for 10 min at RT. The wells were then incubated with 100 μ L of 0.2 mg/mL NeutrAvidin (A2666, ThermoFisher) for 10 min at RT to immobilize the NeutrAvidin on the surface. Then, 100 μ L of 2 μ g/mL biotinylated capture-mAb was introduced to the surface for 10 min at RT. Subsequently, 100 μ L of diluted EV samples were applied and incubated for 10-60 min at RT. Conditioned media were typically diluted 100-fold in PBST-BSA unless otherwise specified with particle/mL concentration, and all human plasma samples were diluted 10-fold in PBST-BSA. For maximal EV capture efficiency, EV incubation was extended to 60 min at RT with shaking at 700 rpm on a 3 mm orbit shaker. Finally, EVs captured on the surface were labeled with 100 μ L of 1 μ g/mL fluorophore-conjugated detector-mAb (or 100 μ L cocktail of 1 μ g/mL fluorophore-conjugated detector-mAbs for multiplexed detection) for 10 min at RT.

A Tecan Fluent 790 liquid handler with a Tecan Hydrospeed plate washer and BioShake plate shakers was used to automate the entire assay process. To account for instrument differences in orbital radius (3 mm vs. 2 mm), the shaking speed was set to 1000 rpm when using the BioShake system. Aside from the shaking speed adjustment, all assay conditions and workflow steps were performed identically during automation.

Single-EV image acquisition and analysis

The prepared samples were immediately imaged using an epi-fluorescence microscope (Nikon Ti2-E) equipped with an electron-multiplying charge-coupled device (EMCCD, iXon Life 888, Andor) and a multi-color laser light engine (CELESTA, Lumencor). A 60× 1.49 NA oil immersion objective (Nikon) was used to detect signals from fluorophore-labeled single EVs with a multi-band excitation filter, emission filter, and dichroic mirror (FF01-391/477/549/639/741 for excitation filter, FF01-441/511/593/684/817 for emission filter, and FF421/491/567/659/776-Di01 for dichroic mirror, Semrock) for the wavelengths of the CELESTA light engine. The images of cell culture-derived EVs were taken with a 50 EM-gain and 50 ms exposure time with varying laser intensities (0.1% - 1.5% of ~800 mW laser output powers) for different targets, fluorophores, and detector-mAbs. For example, mEm-CD9-EVs labeled with CF-568 anti-CD9 detector were excited with 0.3% power of 471 nm laser and 0.3% power of 568 nm laser, whereas recombinant-CD9-His protein labeled with AF-647 anti-His detector was excited with 1.5% power of 637 nm laser. The images of all human plasma-derived EVs were taken with a 50 EM-gain and 50 ms exposure time with 1.5% power of 568 nm and 637 nm lasers. A single frame (snapshot) was taken from each field, and 9 to 49 fields were taken per sample from the center of wells. Micromanager (μ Manager), an open-source image acquisition software, was used to automate the entire image acquisition process via a custom Python script through the Pycro-Manager Python package. The numbers, X and Y coordinates, and intensities of single-EV fluorescence signals in the acquired images were then analyzed using the Thunderstorm ImageJ plugin via a custom Python script through either the PyImageJ Python package or Jython scripting. For co-localization analysis of signals acquired from more than two fluorescence channels, fluorescence signals from different wavelengths located within 2 pixels (~288.8 nm) were considered co-localized. Full-size images (1024×1024 pixels) were used for analysis, while cropped and magnified regions (300×300 pixels represent a 43 μ m x 43 μ m region) were shown in figures for clearer presentation of individual EV signals.

Recombinant-EV production

Recombinant EVs expressing mEmerald-CD9 (mEm-CD9-EVs) or mCherry inserted in the short extracellular loop (SEL) of CD9 (CD9-SEL-mCh-EVs) were produced using the Expi293 protein expression kit (A14635, ThermoFisher) by transiently transfecting the following plasmids. The plasmid for mEm-CD9 expression was a gift from Michael Davidson (Addgene plasmid # 54029; <http://n2t.net/addgene:54029>; RRID: Addgene_54029), and the plasmid for CD9-SEL-mCh-EVs was designed by modifying the pCMV-Sport6-CD9-pHluorin plasmid, a gift from DM Pegtel (Addgene plasmid # 130905; <http://n2t.net/addgene:130905>; RRID: Addgene_130905). The pHluorin-coding sequence was replaced with an mCherry-coding sequence (GenBank ID:

AY678264.1), and the construct was synthesized and cloned into a pTwist CMV vector by Twist Bioscience (Clonal gene synthesis, Twist Bioscience). Expi293 cells (A14635, Gibco) were cultured and transfected with Expifectamine according to the manufacturer's protocol in a 125 mL Erlenmeyer flask (Corning), and the resulting media were collected 48 hours after the transfection and processed to remove cells and debris. Briefly, cells were pelleted by centrifugation at 500 x g at 4°C for 5 min, and then the supernatant was collected and centrifuged again at 3,000 x g at 4°C for 20 min to remove large debris. The supernatant was filtered using a 0.45 µm PES syringe filter followed by a 0.22 µm PES syringe filter (13-1001-05 and 13-1001-04, Fisher Scientific). The filtered media, also mentioned as conditioned media, were analyzed using NTA, and aliquots of the EV-containing media were stored at -80°C. The plasmids used for the recombinant-EV production will be available by contacting the corresponding author.

Human sample handling

All plasma samples were prepared from whole blood collected in K₂-EDTA tubes. BioIVT samples were centrifuged at 4,300-5,000 x g for 10-15 min at 5°C, and plasma fractions were collected using a plasma extractor. MGB samples were centrifuged twice at 2,465-2,600 x g for 15 min at 4°C, and the plasma fractions were aliquoted into 0.5 mL volumes. MGB samples were processed within 2-4 hours of collection. No handling time information was available for the BioIVT samples. All samples were stored at -80°C and, once thawed, they were used for analysis on the same day without refreezing. For single-EV analysis, plasma samples were thawed at RT for approximately 2 h and directly applied to the prepared single-EV analysis surfaces after a 10-fold dilution with PBS pH 7.4, without any additional pre-treatment such as centrifugation or filtration. All plasma samples were analyzed for protein concentration (A280), hemolysis (A410), icterus (A450), and lipemia (A700) (**Supplementary Table 2**). The samples were diluted 50-fold with PBS pH 7.4 for A280 measurement and 5-fold with PBS pH 7.4 for A410, A450, and A700 measurements. The number of patient-derived samples was determined by the availability of well-characterized samples from the MGB Biobank. Although no formal analysis was performed, the sample size was larger than that of comparable published studies and was sufficient to detect statistically significant differences between groups. All human samples were randomly assigned to plates, and analyses were conducted using the automated image analysis workflows to minimize bias. Leftover samples were discarded after the analyses and have never been refrozen once thawed.

Simoa assay

Simoa assay was performed using the Simoa Homebrew Assay Development kit (101361, Quanterix) and an HD-X (Quanterix) instrument according to the manufacturer's protocol. CD9 (EPR23105-125 clone, Abcam) monoclonal antibody was used to capture, CD9 (TS9 clone, Abcam) monoclonal antibody was used to detect, and recombinant CD9 protein (ab152262, Abcam) was used as the standard. For each measurement, samples were incubated with 25 µL of prepared CD9 capture beads and 20 µL of biotinylated detector antibody for 35 min. Samples were washed 6 times with Wash Buffer 1 (Quanterix) and incubated with 100 µL of 120 pM streptavidin-labeled β-galactosidase. Finally, the samples were washed 6 times with wash buffer, resuspended in 25 µL of resorufin β-d-galactopyranoside (Quanterix), and loaded into the microwell array disc.

Reproducibility and statistical analysis

Experimental results for the recombinant EVs (mEm-CD9-EVs and CD9-SEL-mCh-EVs) for Figures 2, 3, and 4a-c represent a single experiment. Similar results with consistent trends were independently reproduced multiple times; however, data from different experiments were not combined, as minor variations were observed across recombinant EV batches. Bars and points indicate mean values, and error bars represent the standard deviation (SD) from nine fields of view within a single well.

Experimental results for human plasma samples represent the means of triplicate measurements for each plasma sample. All samples were analyzed on plates prepared in the same surface passivation batch. The error bars in these experiments represent the SD of the different plasma samples in the groups.

Statistical analyses were performed using Python (v3.12.10) with the SciPy (v1.14.1) and statsmodels (v0.14.4) libraries or GraphPad Prism (v10.4.1) software. The difference between the two groups was tested using a two-tailed Student's T-test or two-tailed Mann-Whitney U test, and differences between the three groups were tested using the Kruskal-Wallis test followed by two-tailed Dunn's post hoc test with Holm correction for multiple comparisons. *p*-values are provided directly in the figures. The correlations between measurements were analyzed using Spearman's rank correlation coefficients (ρ), and full coefficient matrices were visualized as heatmaps with corresponding *p*-values shown in parentheses. Lastly, multiple linear regression between the EV counts and clinical variables was analyzed using ordinary linear regression or robust regression with Huber's estimator based on the normality of the data.

Data Availability

All data supporting the findings of this study are available within the main text, Supplementary Information, and Source Data files.

Code availability

Example Python and ImageJ scripts for image acquisition, image processing, and data analysis are available: https://github.com/Walt-Lab/HT_Single-EV⁴⁹.

References

1. Théry, C., Zitvogel, L. & Amigorena, S. Exosomes: composition, biogenesis and function. *Nat. Rev. Immunol.* **2**, 569–579 (2002).
2. Couch, Y. *et al.* A brief history of nearly EV-erything – The rise and rise of extracellular vesicles. *Journal of Extracellular Vesicles* vol. 10 Preprint at <https://doi.org/10.1002/jev2.12144> (2021).
3. Kalluri, R. & LeBleu, V. S. The biology, function, and biomedical applications of exosomes. *Science* vol. 367 Preprint at <https://doi.org/10.1126/science.aau6977> (2020).
4. van Niel, G., D'Angelo, G. & Raposo, G. Shedding light on the cell biology of extracellular vesicles. *Nat. Rev. Mol. Cell Biol.* **19**, 213–228 (2018).
5. Vlassov, A. V., Magdaleno, S., Setterquist, R. & Conrad, R. Exosomes: Current knowledge of their composition, biological functions, and diagnostic and therapeutic potentials. *Biochimica et Biophysica Acta - General Subjects* vol. 1820 Preprint at <https://doi.org/10.1016/j.bbagen.2012.03.017> (2012).
6. Margolis, L. & Sadovsky, Y. The biology of extracellular vesicles: The known unknowns. *PLoS Biol.* **17**, 1–12 (2019).
7. Kowal, J. *et al.* Proteomic comparison defines novel markers to characterize heterogeneous populations of extracellular vesicle subtypes. *Proc. Natl. Acad. Sci. U. S. A.* **113**, E968–E977 (2016).
8. Ferguson, S. W. & Nguyen, J. Exosomes as therapeutics: The implications of molecular composition and exosomal heterogeneity. *Journal of Controlled Release* **228**, 179–190 (2016).
9. Welsh, J. A. *et al.* Minimal information for studies of extracellular vesicles (MISEV2023): From basic to advanced approaches. *J. Extracell. Vesicles* **13**, (2024).
10. Chiang, C. Y. & Chen, C. Toward characterizing extracellular vesicles at a single-particle level Tse-Hua Tan. *J. Biomed. Sci.* **26**, 1–10 (2019).
11. Ma, B. *et al.* Optical Imaging of Single Extracellular Vesicles: Recent Progress and Prospects. *Chemical and Biomedical Imaging* vol. 2 27–46 Preprint at <https://doi.org/10.1021/cbmi.3c00095> (2024).

12. Han, C. *et al.* Single-vesicle imaging and co-localization analysis for tetraspanin profiling of individual extracellular vesicles. *J. Extracell. Vesicles* **10**, (2021).
13. Lee, K. *et al.* Multiplexed Profiling of Single Extracellular Vesicles. *ACS Nano* **12**, 494–503 (2018).
14. Nguyen, L. T. H. *et al.* An immunogold single extracellular vesicular RNA and protein (AuSERP) biochip to predict responses to immunotherapy in non-small cell lung cancer patients. *J. Extracell. Vesicles* **11**, (2022).
15. Saftics, A. *et al.* Single Extracellular Vesicle Nanoscopy-Universal Protocol (SEVEN-UP): Accessible Imaging Platform for Quantitative Characterization of Single Extracellular Vesicles. *Anal. Chem.* **97**, 1654–1664 (2025).
16. Spitzberg, J. D. *et al.* Multiplexed analysis of EV reveals specific biomarker composition with diagnostic impact. *Nat. Commun.* **14**, (2023).
17. Su, Y., He, W., Zheng, L., Fan, X. & Hu, T. Y. Toward Clarity in Single Extracellular Vesicle Research: Defining the Field and Correcting Missteps. *ACS Nano* vol. 19 16193–16203 Preprint at <https://doi.org/10.1021/acsnano.5c00705> (2025).
18. Imanbekova, M., Sharma, M. & Wachsmann-Hogiu, S. On the dilemma of using single EV analysis for liquid biopsy: the challenge of low abundance of tumor EVs in blood. *Theranostics* vol. 15 8031–8048 Preprint at <https://doi.org/10.7150/thno.115131> (2025).
19. Shivanandan, A., Deschout, H., Scarselli, M. & Radenovic, A. Challenges in quantitative single molecule localization microscopy. *FEBS Letters* vol. 588 Preprint at <https://doi.org/10.1016/j.febslet.2014.06.014> (2014).
20. Van Deun, J. *et al.* EV-TRACK: Transparent reporting and centralizing knowledge in extracellular vesicle research. *Nat. Methods* **14**, 228–232 (2017).
21. Sharma, S., LeClaire, M., Wohlschlegel, J. & Gimzewski, J. Impact of isolation methods on the biophysical heterogeneity of single extracellular vesicles. *Sci. Rep.* **10**, (2020).
22. Carney, R. P. *et al.* Harnessing extracellular vesicle heterogeneity for diagnostic and therapeutic applications. *Nature Nanotechnology* vol. 20 14–25 Preprint at <https://doi.org/10.1038/s41565-024-01774-3> (2025).

23. Gidi, Y., Bayram, S., Ablenas, C. J., Blum, A. S. & Cosa, G. Efficient One-Step PEG-Silane Passivation of Glass Surfaces for Single-Molecule Fluorescence Studies. *ACS Appl. Mater. Interfaces* **10**, (2018).
24. Jo, S. & Park, K. Surface modification using silanated poly(ethylene glycol)s. *Biomaterials* **21**, (2000).
25. Jain, A. *et al.* Probing cellular protein complexes using single-molecule pull-down. *Nature* **473**, 484–488 (2011).
26. Nishida-Aoki, N. *et al.* Disruption of Circulating Extracellular Vesicles as a Novel Therapeutic Strategy against Cancer Metastasis. *Molecular Therapy* **25**, 181–191 (2017).
27. Saftics, A. *et al.* Single Extracellular Vesicle Nanoscopy. *J. Extracell. Vesicles* **12**, (2023).
28. Rissin, D. M. *et al.* Single-molecule enzyme-linked immunosorbent assay detects serum proteins at subfemtomolar concentrations. *Nat. Biotechnol.* **28**, 595–599 (2010).
29. Torres-Acosta, M. A., Lye, G. J. & Dikicioglu, D. Automated liquid-handling operations for robust, resilient, and efficient bio-based laboratory practices. *Biochem. Eng. J.* **188**, (2022).
30. Pinkard, H. *et al.* Pycro-Manager: open-source software for customized and reproducible microscope control. *Nature Methods* vol. 18 Preprint at <https://doi.org/10.1038/s41592-021-01087-6> (2021).
31. Ovesný, M., Křížek, P., Borkovec, J., Švindrych, Z. & Hagen, G. M. ThunderSTORM: A comprehensive ImageJ plug-in for PALM and STORM data analysis and super-resolution imaging. *Bioinformatics* **30**, (2014).
32. Cvjetkovic, A. *et al.* Detailed Analysis of Protein Topology of Extracellular Vesicles- Evidence of Unconventional Membrane Protein Orientation. *Sci. Rep.* **6**, (2016).
33. Johnsen, K. B., Gudbergsson, J. M., Andresen, T. L. & Simonsen, J. B. What is the blood concentration of extracellular vesicles? Implications for the use of extracellular vesicles as blood-borne biomarkers of cancer. *Biochimica et Biophysica Acta - Reviews on Cancer* vol. 1871 Preprint at <https://doi.org/10.1016/j.bbcan.2018.11.006> (2019).

34. Noren Hooten, N., Byappanahalli, A. M., Vannoy, M., Omoniyi, V. & Evans, M. K. Influences of age, race, and sex on extracellular vesicle characteristics. *Theranostics* vol. 12 Preprint at <https://doi.org/10.7150/thno.72676> (2022).
35. Eitan, E. *et al.* Age-Related Changes in Plasma Extracellular Vesicle Characteristics and Internalization by Leukocytes. *Sci. Rep.* **7**, (2017).
36. Grenier-Pleau, I. *et al.* Blood extracellular vesicles from healthy individuals regulate hematopoietic stem cells as humans age. *Aging Cell* **19**, (2020).
37. Bebelman, M. P., Smit, M. J., Pegtel, D. M. & Baglio, S. R. Biogenesis and function of extracellular vesicles in cancer. *Pharmacology and Therapeutics* vol. 188 Preprint at <https://doi.org/10.1016/j.pharmthera.2018.02.013> (2018).
38. Kumar, M. A. *et al.* Extracellular vesicles as tools and targets in therapy for diseases. *Signal Transduction and Targeted Therapy* vol. 9 Preprint at <https://doi.org/10.1038/s41392-024-01735-1> (2024).
39. Bebelman, M. P., Janssen, E., Pegtel, D. M. & Crudden, C. The forces driving cancer extracellular vesicle secretion. *Neoplasia (United States)* vol. 23 Preprint at <https://doi.org/10.1016/j.neo.2020.11.011> (2021).
40. Ricklefs, F. L. *et al.* Circulating extracellular vesicles as biomarker for diagnosis, prognosis, and monitoring in glioblastoma patients. *Neuro. Oncol.* **26**, 1280–1291 (2024).
41. Melo, S. A. *et al.* Glypican-1 identifies cancer exosomes and detects early pancreatic cancer. *Nature* **523**, (2015).
42. Peinado, H. *et al.* Melanoma exosomes educate bone marrow progenitor cells toward a pro-metastatic phenotype through MET. *Nat. Med.* **18**, (2012).
43. Graham, R. *et al.* Serum-derived extracellular vesicles from breast cancer patients contribute to differential regulation of T-cell-mediated immune-escape mechanisms in breast cancer subtypes. *Front. Immunol.* **14**, (2023).
44. Menck, K. *et al.* Characterisation of tumour-derived microvesicles in cancer patients' blood and correlation with clinical outcome. *J. Extracell. Vesicles* **6**, (2017).

45. Imanbekova, M., Sharma, M. & Wachsmann-Hogiu, S. On the dilemma of using single EV analysis for liquid biopsy: the challenge of low abundance of tumor EVs in blood. *Theranostics* **15**, 8031–8048 (2025).
46. Sharma, R., Huang, X., Brekken, R. A. & Schroit, A. J. Detection of phosphatidylserine-positive exosomes for the diagnosis of early-stage malignancies. *Br. J. Cancer* **117**, (2017).
47. Ferguson, S. & Weissleder, R. Modeling EV Kinetics for Use in Early Cancer Detection. *Adv. Biosyst.* **4**, (2020).
48. Mizenko, R. R. *et al.* Tetraspanins are unevenly distributed across single extracellular vesicles and bias sensitivity to multiplexed cancer biomarkers. *J. Nanobiotechnology* **19**, 250 (2021).
49. Han, C., Melkonian, A., Rolando, J., Whiteman, S. & Walt, D. High-throughput single extracellular vesicle imaging platform for direct extracellular vesicle profiling of human plasma. Preprint at <https://doi.org/10.5281/zenodo.19199436> (2026).

Acknowledgments

We acknowledge members of the Walt lab for helpful discussions and, in particular, Dmitry Ter-Ovanesyan for critical feedback and discussion and Daniel Portal for his efforts in general laboratory management. This work was funded by the NIH Center for Alzheimer's and Related Dementias (1ZIAAG000544-03, DRW), Open Philanthropy Project/Good Ventures (DRW), and the Wyss Institute for Biologically Inspired Engineering (DRW). CH was partially supported by the National Research Foundation of Korea (NRF) grant funded by the Korea government (MSIT) (RS-2024-00393195, CH). AVM was partially supported by the Brigham and Women's Hospital (BWH) Department of Pathology T32 Oncopathology Training Program (OTP) (T32CA251062, AVM).

Author contributions

CH conceptualized the study. CH and AVM performed experiments using recombinant EVs and analyzed data. CH, AVM, and JCR performed experiments using human samples and analyzed data. SW performed Simoa assays and analyzed the data. DRW supervised the study. CH wrote the manuscript, and all authors read, edited, and approved the final manuscript.

Competing Interests

DRW has a financial interest in Quanterix Corporation; he is an inventor of the Simoa technology, a founder of the company, and serves on its Board of Directors. DRW's interests were reviewed and are managed by Mass General Brigham (MGB) and Harvard University in accordance with their conflict-of-interest policies. CH, AVM, and DRW have filed IP on methods for high-throughput single-EV imaging analysis (63/845,578). The remaining authors declare no competing interests.

Figure 1. Overview and representative workflow of single-EV imaging analysis.

High-throughput platforms with glass bottoms, such as 96-well glass-bottom plates or 18-chambered microscope slides, are functionalized with polyethylene glycol (PEG) and biotin-PEG and stored at -20 °C until use. The single-EV capture and detection workflow is almost identical to a conventional sandwich immunoassay. Captured and labeled EVs on the surface are imaged using an epi-fluorescence microscope equipped with an electron multiplying charge-coupled device (EMCCD) camera that can detect dim signals from single molecules. The single-EV fluorescence signals are extracted from the acquired images using custom scripts via open-source software, including ImageJ packages and Python libraries. The scheme was created with BioRender.com.

ARTICLE IN PRESS

Figure 2. Assessment of single-EV detection specificity.

(a) Schematic of recombinant EV production expressing fluorescent protein-tagged CD9. mEm-CD9-EVs express mEmerald proteins in the cytosolic region of the membrane, and CD9-SEL-mCh-EVs express mCherry proteins on the extracellular side of the membrane. **(b)** Overview of EV-specific detection strategy using the same anti-CD9 mAbs for both capture and detection. **(c)** Representative single-EV images of a mixture containing mEm-CD9-EVs and soluble CD9-His recombinant proteins, and **(d)** colocalization analysis of anti-CD9 detector-mAb signals (green) with either mEm-CD9-EVs (blue) or soluble CD9-His protein signals (red) for the assessment of detection specificity. The size of micrographs is 43 μm x 43 μm . Bars represent mean \pm standard deviation (SD), with $n = 9$ fields of view. **(e)** Schematic of specific detection of spiked-in EVs in a human plasma sample. A human plasma sample spiked with CD9-SEL-mCh-EVs was analyzed using surfaces functionalized with either mCherry-capture or CD9-capture mAbs. **(f)** Representative single-EV images acquired from the mCherry-capture surface (top) and CD9-capture surface (bottom), and **(g, h)** corresponding colocalization analyses. CD9-SEL-mCh-EVs were detected in yellow (indicating colocalization of green from anti-CD9 detector-mAb and red from mCherry), while plasma-derived CD9⁺ EVs were detected in green (anti-CD9 detector-mAb only). The size of micrographs is 43 μm x 43 μm . Bars represent mean \pm SD, with $n = 9$ fields of view. All scale bars are ~ 10 μm . Schemes are created with BioRender.com. Source data are provided as a Source Data file.

Figure 3. Assessment of single-EV detection sensitivity.

(a) Workflow for EV-capture efficiency estimation using CD9 Simoa analysis. CD9 concentrations were measured before and after incubation with either an anti-CD9 capture surface or a no-capture control surface. Capture efficiency was calculated as the fraction of unbound EVs remaining after incubation relative to the input EV concentration. **(b)** Estimated capture efficiency of the anti-CD9 capture surface and the no-capture control surface across different input EV concentrations. Bars represent mean \pm SD, with $n = 3$ wells. **(c)** Workflow for the assessment of single-EV detection sensitivity and dynamic range. A mEm-CD9-EV sample with a predetermined concentration (2.3×10^{11} EVs/mL by nanoparticle tracking analysis) was serially diluted 17 times in 4-fold steps and analyzed using an anti-CD9 capture surface. Signals were detected either as mEmerald+ single-EV counts or bulk mEmerald intensity per field. **(d)** Representative single-EV images of mEm-CD9-EVs at different concentrations and **(e)** quantification of average single-EV counts (red) and bulk intensity (blue) per fields. Solid lines indicate the dynamic ranges, and dashed lines represent the limit of detection (LOD), calculated as mean + $3 \times$ SD of background signals. The circles and triangles indicate the mean, and the error bars indicate SD, with $n = 8$ fields of view. The size of micrographs is $43 \mu\text{m} \times 43 \mu\text{m}$. All scale bars are $\sim 10 \mu\text{m}$. Schemes are created with BioRender.com. Source data are provided as a Source Data file.

Figure 4. High-throughput analysis of normal human plasma samples using an automated single-EV imaging platform

(a) Workflow for automated single-EV imaging analysis in a high-throughput format. Analysis was performed in a 96-well plate using a Tecan Fluent 780 liquid handler equipped with a HydroSpeed plate washer. Imaging was automated using a Nikon Ti2E motorized microscope and a custom Pycro-Manager script. Image processing was automated with custom ImageJ and Python scripts. (b) Intra-plate reproducibility assessment. A mEm-CD9-EV sample was analyzed across all 96 wells of a 96-well plate (plate 1), and average single-EV counts were visualized as a heat map, with $n = 25$ fields of view. (c) Inter-plate reproducibility assessment. The same mEm-CD9-EV sample was analyzed on a second plate, and the results were compared with plate 1. Each dot represents a single well. Bars indicate SD, with $n = 96$ wells. p -value was calculated using a two-tailed Student's T-test. (d) Representative single-EV images of 10% pooled human plasma samples analyzed under different control conditions and (e) the quantification of EV counts per field. The size of micrographs is $43 \mu\text{m} \times 43 \mu\text{m}$. Bars represent mean \pm SD, with $n = 25$ fields of view. (f) Single-EV CD9 and CD81 analysis of 96 individual normal human plasma samples. Dots represent individual plasma samples. Bars represent mean \pm SD, with $N = 96$ individual plasmas. p -value was calculated using a two-tailed Mann-Whitney U test. (g) Heatmap of two-tailed Spearman correlation coefficients (ρ) between EV counts and demographic parameters (sex, age, BMI). Blocks and numbers represent Spearman ρ , and numbers in parentheses indicate corresponding p -values, with $N = 96$ individual plasmas. All scale bars are $\sim 10 \mu\text{m}$. The scheme was created with BioRender.com. Source data are provided as a Source Data file.

Figure 5. High-throughput analysis of breast cancer plasma samples using an automated single-EV imaging platform

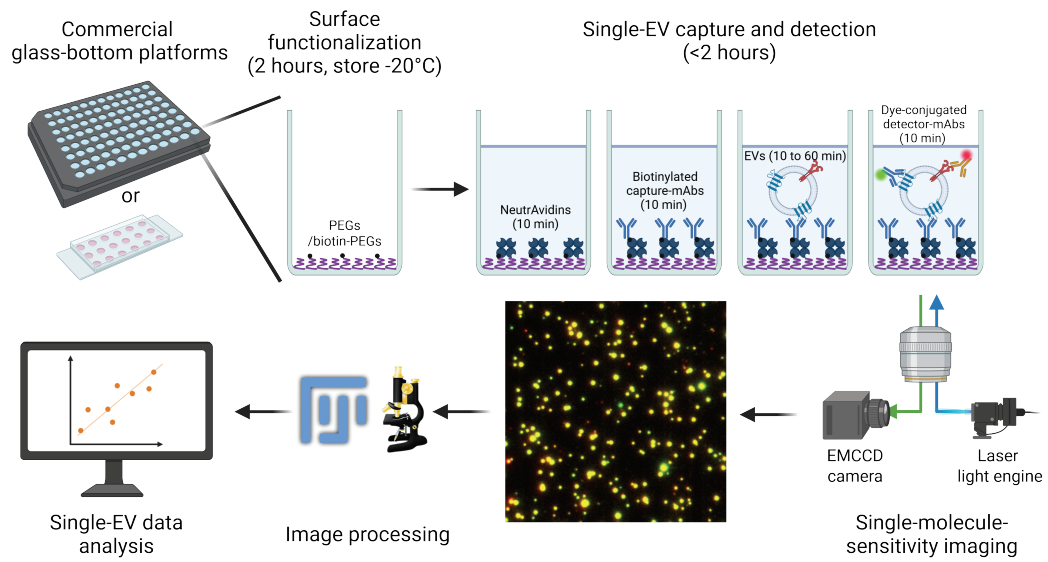
(a) Stratification of breast cancer samples by disease stage. (b) CD9⁺ and (c) CD81⁺ EV levels in plasma samples from breast cancer patients and normal individuals. Brown, orange, blue, and black indicate late-stage, early-stage, normal individuals, and PBS control samples, respectively. Bars represent mean \pm SD, with $n = 3$ replicates. (d) Statistical analysis of plasma CD9⁺ EV levels across disease stage groups using the Kruskal-Wallis test ($p < 0.001$). Bars represent mean \pm SD. N for each group is indicated in panel a. Two-tailed Dunn's post-hoc test indicated significant differences between normal and late-stage groups (adjusted $p < 0.001$), and between early and late-stage groups (adjusted $p = 0.002$). (e) Receiver operating characteristic (ROC) curve analyses of CD9⁺ levels between disease stage groups. Cyan, yellow, and magenta curves represent comparisons between normal vs. early-stage, normal vs. late-stage, and early vs. late-stage groups, respectively. Area under the curve (AUC) values are shown in parentheses. (f) Statistical analysis of plasma CD81⁺ EV levels between disease stage groups using the Kruskal-Wallis test ($p < 0.001$). Bars represent mean \pm SD. N for each group is indicated in panel a. Two-tailed Dunn's post-hoc test revealed a significant difference only between normal and late-stage groups (adjusted $p < 0.001$). (g) ROC curve analyses of CD81⁺ EV levels across disease stage groups. Cyan, yellow, and magenta curves represent comparisons between normal vs. early-stage, normal vs. late-stage, and early vs. late-stage groups, respectively. AUC values are shown in parentheses. Source data are provided as a Source Data file.

NCOMMS-25-62577C – Walt

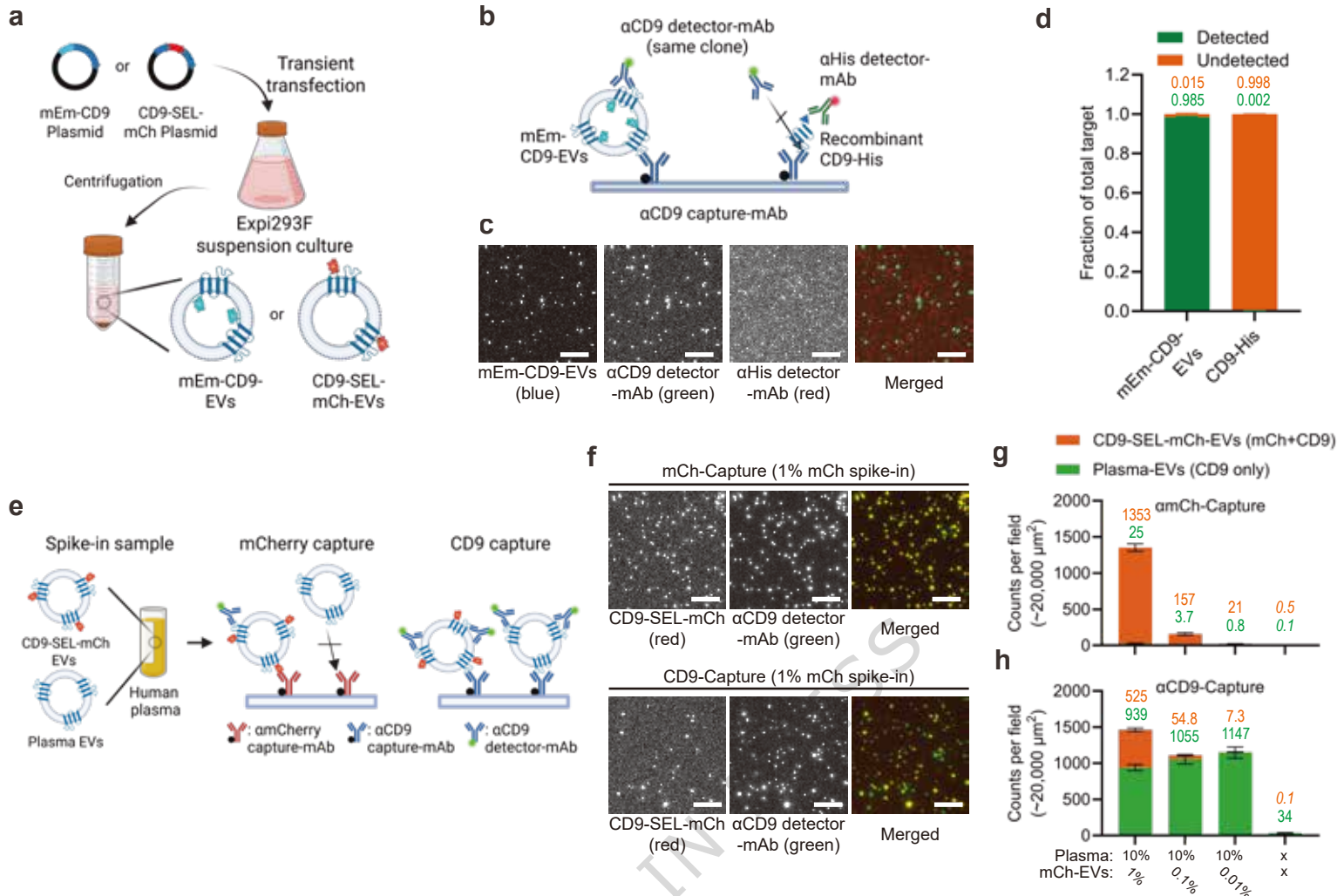
EDITORIAL SUMMARY

Han and colleagues present a high-throughput platform to analyse individual extracellular vesicles (EVs) directly from unprocessed clinical samples. The approach enables precise and large-scale analysis of EVs for clinical applications.

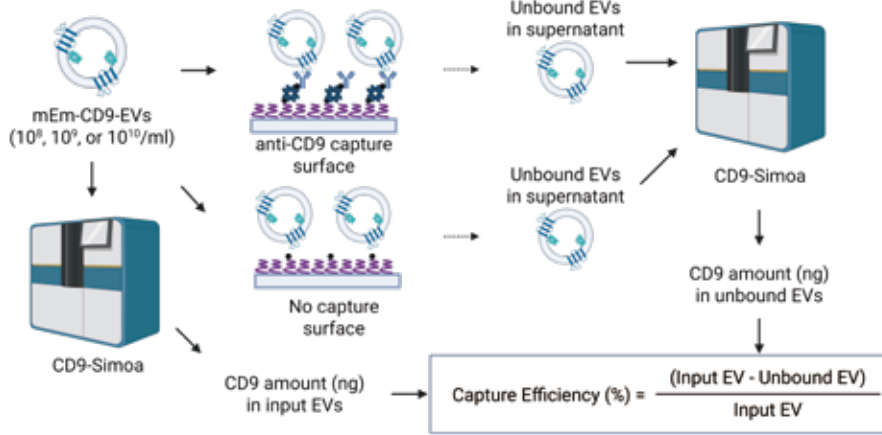
Peer Review Information: *Nature Communications* thanks Sherri Christian and the other, anonymous, reviewer(s) for their contribution to the peer review of this work. A peer review file is available.



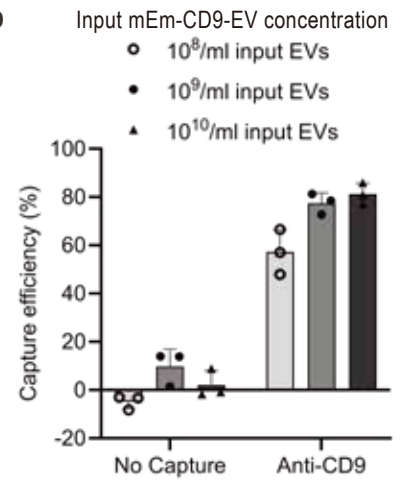
ARTICLE IN PRESS



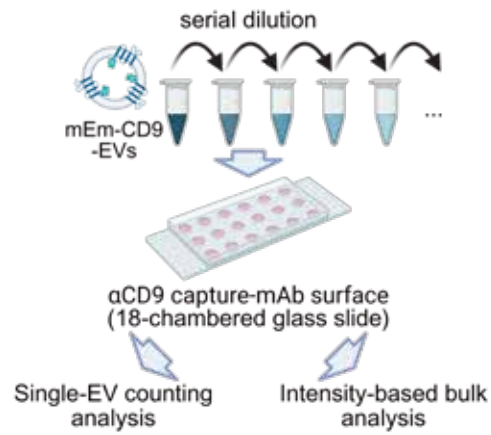
a



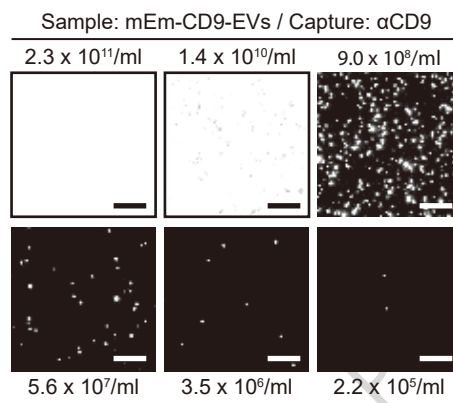
b



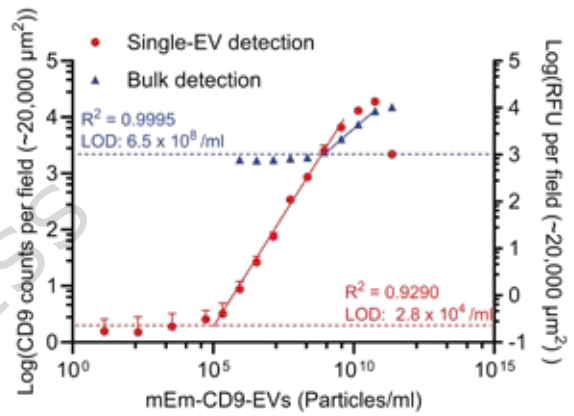
c

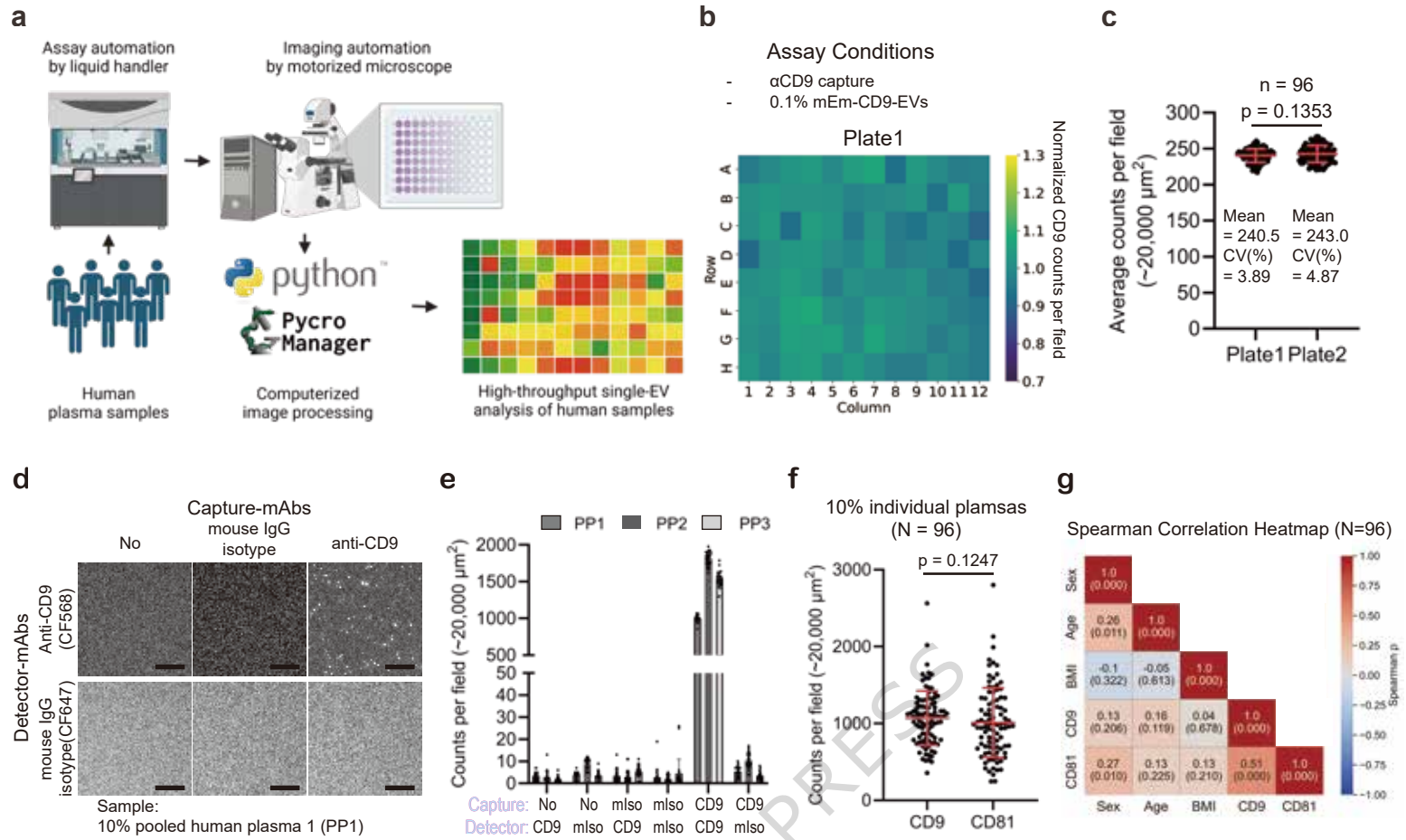


d



e





ARTICLE IN PRESS

